

Earth ArXiv

This is a non-peer-reviewed preprint submitted to EarthArXiv.

This manuscript has been submitted for publication in the *Journal of Atmospheric and Oceanic Technology*. Please note the manuscript has yet to be formally accepted for publication. Subsequent versions of this manuscript may have slightly different content. If accepted, the final version of this manuscript will be available via the 'Peer-reviewed Publication DOI' link on the right-hand side of this webpage. Please feel free to contact any of the authors; we welcome feedback.

1 **The Motion and Tilts of Subsurface Floats due to Surface Waves**

2 Eric A. D'Asaro^{ab} and Andrey Y. Shcherbina^a

3 ^a *Applied Physics Laboratory, University of Washington, Seattle, WA, USA*

4 ^b *School of Oceanography, University of Washington*

5 *Corresponding author:* Eric A D'Asaro, dasaro@apl.washington.edu

6 ABSTRACT: Subsurface and nearly neutrally-buoyant floats can be stable, well-behaved platforms
7 for measuring ocean dynamics in the near-surface wave zone. Here we measure and model the
8 tilt of such platforms due to the waves using data from Lagrangian floats built at the Applied
9 Physics Laboratory (APL/UW) and carrying a Nortek Signature 1000 Current Profiler with an
10 AHRS (Attitude and Heading Reference System). We analyze carefully chosen data segments
11 where the wave-induced tilts are finite but small and the float does not rotate significantly, in
12 a two-dimensional, depth-downwave coordinate system assuming small tilts and linear surface
13 wave dynamics. By combining the constraints due to geometry, a wave-following float, and wave
14 dynamics, we link measurements of both linear and angular acceleration to measure the tilts to an
15 accuracy of a few tenths of a degree and simultaneously show that the data is consistent with the
16 analysis assumptions. This is confirmed by swinging the AHRS on pendulums in the laboratory.
17 The same tests disturbingly indicate that the tilts produced by the AHRS can have large errors for
18 tilts larger than a few degrees. The tilt is predicted to an accuracy of about 10% from the wave
19 properties by a 3-parameter linear dynamical model calibrated with field data. The waves force tilt
20 through their horizontal acceleration and through their strain exerting torques on the float. These
21 floats are a somewhat underdamped oscillator (Quality Factor=3, resonance at 3 second period)
22 and will exhibit a decaying oscillation of a few cycles when perturbed.

23 SIGNIFICANCE STATEMENT: Accurate measurements of the ocean near the surface often
24 require a detailed understanding of the motion of the platform caused by waves. Here, we model
25 the vertical and horizontal motion and tilts of a subsurface oceanographic float near the surface
26 and tune the model parameters using field data aided by laboratory measurements.

27 **1. Introduction**

28 The upper few meters of the ocean are an important region for horizontal transport, air-sea
29 exchange, surface wave dynamics, and the interpretation of remote sensing data. Although near-
30 surface currents are routinely measured by the global array of surface drifters (Centurioni et al.
31 2019), simulated by operational and research models (Menemenlis et al. 2008) and thousands of
32 papers describe ocean 'surface' currents, detailed current measurements in the top few meters
33 remain limited and a clear understanding of the structure of velocity in this region remains an
34 area of active research, e.g. Laxague et al. (2018), Pizzo et al. (2019). The prospect of global
35 surface current measurements by satellite (Ardhuin et al. 2019; Wineteer et al. 2020; Torres et al.
36 2023) makes the development of complementary measurement techniques particularly timely. For
37 in situ measurements, surface waves usually result in motion and tilting of the measurement
38 platform and possible contamination of the measurement by platform wakes. These factors are
39 particularly detrimental to near-surface current measurements because the wave velocities are
40 typically much larger than the low-frequency velocities and can often not be removed by averaging
41 alone due to nonlinearities intrinsic in the measurement system or induced by the platform motion
42 or wakes. Shcherbina and D'Asaro (2025), following earlier work (Pollard 1973; Amador et al.
43 2017; Thomson et al. 2019), analyze this problem in detail for a variety of platforms.

44 Neutrally buoyant (Gould 2005) and profiling (Wenstrand 1979; Luyten and Swallow 1976)
45 floats have been used since the 1960s to measure ocean currents and current profiles. Currents
46 are measured from the motion of acoustically tracked floats or from the voltage across the float
47 induced by the water's motion through the geomagnetic field (Sanford et al. 1978). Floats are
48 also attractive platforms for near-surface measurement. Since they move with the water, they can
49 safely operate in even the most severe weather (D'Asaro and McNeil 2007) and can easily profile
50 very near the surface. Operated as water-following Lagrangian instruments (D'Asaro 2003), they
51 naturally measure vertical velocity from their own motion. Equipped with acoustic Doppler current

52 profilers (ADCPs), they can measure relative horizontal velocities and absolute vertical velocities
53 (Kumar et al. 2019; D’Asaro et al. 2018; Shcherbina et al. 2019). Below the influence of surface
54 waves, floats are very stable with typical RMS tilts of a fraction of a degree, which introduces
55 only small errors into ADCP velocity measurements. However, surface waves induce oscillatory
56 motion and tilt as a float approaches the surface. Shcherbina and D’Asaro (2025) show that these
57 lead to measurement errors comparable to the Stokes drift of the surface wave.

58 In this paper, we model the displacement and tilting of Lagrangian floats in the upper ocean due
59 to surface waves. A following paper will compute the resulting errors in horizontal and vertical
60 velocity as measured by an ADCP on the float. Section 2 reviews the basic properties of surface
61 waves relevant to this analysis. Section 3 derives kinematic relationships for different types of tilt
62 measurements made on a float forced by surface waves. Section 4 describes the ocean measurements
63 and summarizes laboratory measurements described in more detail in the Supplementary Material
64 (henceforth SM). Section 5 analyzes these data by evaluating their accuracy and consistency with
65 the analysis assumptions. Section 6 formulates a model of float tilt and evaluates it for the data.
66 Section 7 summarizes these results. Section 8 discusses them.

67 **2. Wave Properties**

68 *a. Basic Equations*

69 As in D’Asaro (2015), we follow Phillips (1977) (P77) section 3.2 and D’Asaro (2015) and specify
70 a two-dimensional deep water surface wave by its vertical surface displacements (P77 3.2.1)

$$\zeta = \mathbf{a} \cos(kx - \omega t) \quad (1)$$

71 where \mathbf{a} is the wave amplitude, $\omega^2 = gk$ and g is the magnitude of gravitational acceleration. The
72 velocity potential (P77, 3.2.4) is

$$\phi = \mathbf{a} \frac{\omega}{k} e^{kz} \sin(kx - \omega t) \quad (2)$$

73 where z is the vertical coordinate and positive up. Velocity $\vec{u} = \vec{\nabla}\phi$ (P77, 2.4.19) so

$$u = \alpha \omega e^{kz} \cos(kx - \omega t) \quad (3)$$

$$w = \alpha \omega e^{kz} \sin(kx - \omega t) \quad (4)$$

74 and accelerations in the \hat{x} and \hat{z} directions are

$$a_x = \frac{\partial u}{\partial t} = \alpha \omega^2 e^{kz} \sin(kx - \omega t) \quad (5)$$

$$a_z = \frac{\partial w}{\partial t} = -\alpha \omega^2 e^{kz} \cos(kx - \omega t). \quad (6)$$

75 A consistency check is that (6) is $\partial^2/\partial t^2$ of (1). To first order in the small parameter αk , the
76 displacements of particles from initial positions x_0 and z_0 are

$$\chi = \int_0^t u(\vec{x}_0, t) dt = -\alpha e^{kz} \sin(kx - \omega t) \quad (7)$$

77

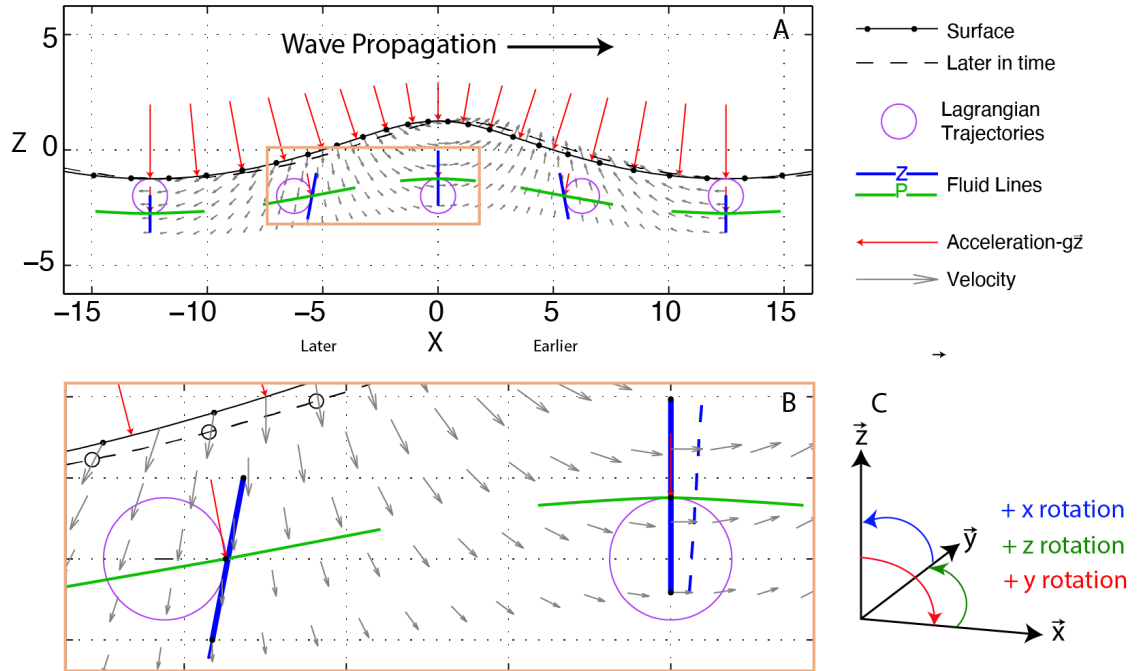
$$\xi = \int_0^t w(\vec{x}_0, t) dt = \alpha e^{kz} \cos(kx - \omega t) \quad (8)$$

78 respectively, where comparison of (8) and (1) provides another consistency check.

79 The resulting wave surface, velocity vectors, Lagrangian trajectories, and the distortion of fluid
80 lines are shown in Fig. 1 along with the definition of the full 3D coordinate system.

81 *b. Wave Tilt and Strain Kinematics*

82 The analysis will study the tilts of the float induced by surface waves assuming that all angles
83 are small and the surface waves are linear, both of which will be satisfied if the wave slope is
84 small. The analysis will follow the mathematical convention (Fig. 1C) using the right-hand rule to
85 define angles with $+z$ pointing upward. Thus, positive angles in the $x - z$ plane appear clockwise
86 when viewed looking in the $+y$ direction as in Fig. 1C and positive angles in the $x - y$ plane
87 are anti-clockwise when viewed from above. The acceleration of gravity has a magnitude g and
88 a vector $\vec{g} = -g\hat{z}$, so that a free-falling particle accelerates downward with $\vec{a} = \vec{g}$ and $a_z = -g$.
89 We assume that accelerations are much less than g , so all angles are small and we keep only the
90 lowest-order terms in tilt.



91 FIG. 1. A) and B) Kinematics of a monochromatic linear surface wave. B) is zoom of orange box in A).
 92 The Wave propagates in the $+x$ direction, to the right. Wave phase varies horizontally with a wavelength of
 93 25. The black line with dots marks the surface; the dashed black line shows the surface at a somewhat later
 94 time. Red lines mark the direction of effective gravity (\vec{g}), i.e. gravitational acceleration + fluid acceleration.
 95 These are perpendicular to pressure surfaces; at the water surface they are perpendicular to the surface. Circles
 96 (purple) show representative Lagrangian trajectories of fluid parcels. Green lines at 5 different locations show
 97 the positions of fluid lines of constant pressure. These lines are nearly horizontal and will be called the 'P-lines'.
 98 Lagrangian particles follow surfaces of constant pressure to at least second order (D'Asaro 2015) so the P-lines
 99 also mark the motion of a nearly horizontal line of particles. Blue lines mark lines of fluid that would be vertical
 100 at the top of the wave; they will be 'Z-lines'. The P-lines and the surface remain perpendicular to the direction
 101 of the effective gravity, while the Z-lines tilt in the opposite direction with the same magnitude. The changing
 102 angles between the P- and Z-lines illustrates the straining of the fluid by the wave. C) Coordinate definition.
 103 Rotation angles obey the right-hand rule so that a positive rotation angle is clockwise when viewed looking
 104 toward $+y$ as in this figure.

105 In still water, a subsurface float with a stable righting moment will orient itself along \vec{g} , usually
 106 with its longest axis aligned vertically. More generally, its orientation will seek the direction of
 107 local "effective gravity" \vec{g}_e defined as the sum of the gravity \vec{g} and the negative of acceleration

108 vectors

$$\vec{g}_e = \vec{g} - a_x \vec{x} - a_z \vec{z} \quad (9)$$

109 where g is the magnitude of \vec{g} and \vec{x} and \vec{z} are the unit vectors in the x and z directions respectively
110 (Fig. 1c). In this notation, a free-falling particle accelerates at \vec{g} , $a_z = -g$, $a_x = 0$, and $g_e = 0$.

111 The \vec{g}_e vector is shown as the red lines in Fig. 1AB. The angle of \vec{g}_e from $-\vec{z}$ (down) is

$$\theta_G \approx \frac{a_x}{g} = \mathbf{a}k e^{kz} \sin(kx - \omega t). \quad (10)$$

112 In the presence of waves, θ_G on a water-following float continually changes with time thereby
113 causing a float with a righting moment to tilt, as will be investigated in great detail below.

114 The green lines in Fig. 1AB show the tilts of a surface of constant pressure. They will be called
115 'P-lines'. P-lines tilt in the same way as the overlying surface since this is also a surface of constant
116 pressure. To first order, their tilt relative to the horizontal is

$$\theta_P = \frac{\pi}{2} - \frac{\partial \xi}{\partial x} = \frac{\pi}{2} + \mathbf{a}k e^{kz} \sin(kx - \omega t). \quad (11)$$

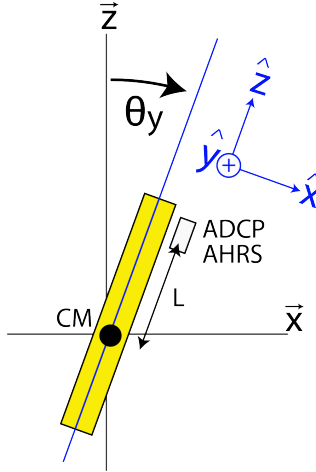
117 θ_P is perpendicular to θ_G , i.e. $\theta_P - \theta_G = \pi/2$.

118 The blue lines in Fig. 1AB show the tilt of a fluid line that would be vertical in the absence of
119 waves. They will be called 'Z-lines'. From (8), their first order tilt is

$$\theta_Z = \frac{\partial \chi}{\partial z} = -\mathbf{a}k e^{kz} \sin(kx - \omega t) = -\theta_G \quad (12)$$

120 θ_Z is exactly equal to $-\theta_G$.

121 The Z- and P-lines tilt in opposite directions with the same magnitude, so that there is no net
122 rotation of a fluid parcel, only straining, as required for potential flow. The tilting of Z-lines
123 corresponds to the 'Inertial' case described by Longuet-Higgins (1986), his figure 21; the tilting
124 of P-lines corresponds to his 'Hydrostatic' case.



125 FIG. 2. Float Tilt Coordinates - a) Float tilts at an angle $\theta = \theta_y$ in the $x - z$ plane defining float coordinates
 126 $(\hat{x}, \hat{y}, \hat{z})$. The tilt is measured by an AHRS unit that is offset along the float by a distance L from the center of
 127 rotation.

128 3. Float and Measurement Kinematics

129 a. Geometry and Notation

130 The displacements of the float are accurately described by χ and ξ , both for fully Lagrangian
 131 floats and for slowly profiling ones, since both the water and the float are accelerated by the
 132 same wave pressure gradients, as discussed in detail by D'Asaro (2003, 2015). Float tilting is
 133 more complex because multiple factors act to tilt the float toward either Z-lines or toward P-lines,
 134 depending on the float geometry. Measuring and modeling the tilt is thus the major task of this
 135 work.

136 Figure 2 shows the geometry of the float tilt measurements in a vertical $x - z$ plane. The float
 137 tilts from the vertical with angle θ_y . The analysis will remain in the $x - z$ plane, so θ is the same as
 138 θ_y . Measurements by an AHRS (see Section 4) of vector acceleration and rotation rate are made a
 139 distance L above the center of rotation. Measured and computed quantities will be represented by
 140 capital letters. Thus, the value of θ computed from the horizontal accelerometers is Θ_A .

141 For each measured quantity, \hat{X} will denote the measured value in the float frame, X the value
 142 in the $(\vec{x}, \vec{y}, \vec{z})$ frame. Physical values, i.e., those described in Section 2, will be represented by
 143 lowercase letters; there is only one real tilt, θ .

144 Measurements in the instrument frame are related to those in the earth's frame by

$$\widehat{X}_z = X_z \cos(\theta) + X_x \sin(\theta) \approx X_z + X_x \theta \quad (13)$$

$$\widehat{X}_x = X_x \cos(\theta) - X_z \sin(\theta) \approx X_x - X_z \theta \quad (14)$$

145 where the approximate formulae apply for small values of θ .

146 *b. Acceleration kinematics*

147 For small tilt angles, the measured acceleration is the sum of the acceleration of the center of the
148 float and the angular acceleration times the lever arm L projected onto the sensor axis

$$\widehat{A}_z = A_z + g \quad (15)$$

$$\widehat{A}_x = A_x + L \frac{d^2\theta}{dt^2} - g\theta. \quad (16)$$

149 A centripetal acceleration term, $L(\frac{d\theta}{dt})^2 \hat{z}$, and terms $A_x \theta$ and $A_z \theta$ are quadratic in tilt and thus
150 ignored. At sufficiently low frequencies, the first and second terms on the RHS of (16) are
151 negligible and the accelerometer accurately measures tilt as $-\widehat{A}_x/g$. More generally, dividing (16)
152 by g yields the angle that would be measured assuming this

$$\Theta_A = \theta - A_x/g - \omega_L^{-2} \frac{d^2\theta}{dt^2} \quad (17)$$

153 where $\omega_L = \sqrt{g/L}$ is the pendulum frequency. Thus, Θ_A does not measure the true tilt, but the sum
154 of the true tilt, a term due to lateral acceleration, and a term due to angular acceleration.

155 It is useful to make a nondimensional vertical acceleration with the same units as an angle,

$$\Phi_Z = A_z/g \quad (18)$$

156 *c. Rotation Rate Kinematics*

157 The rate of rotation around the y axis is

$$\Omega_y = \frac{d\theta}{dt} \quad (19)$$

158 with Ω_z and Ω_x measuring the rotation about the vertical and x axes respectively. The measured
 159 quantity in float coordinates is

$$\widehat{\Omega}_y = \Omega_y + \Omega_z \Theta_x - \Omega_x \Theta_z. \quad (20)$$

160 The last two terms on the right are ignored so that the problem stays in the $x - z$ plane. Integration
 161 in time defines

$$\Theta_Y(T) = \int_0^T \Omega_y(t) dt + \Theta_0 \quad (21)$$

162 with integration constant Θ_0 . Θ_Y thus measures only the fluctuations in float tilt, or in the presence
 163 of low frequency measurement noise, measures the tilt at high, but not at low frequencies. In
 164 contrast, Θ_A accurately measures the tilt at low but not high frequencies (17). Combining these,
 165 sensor fusion, yields measurements at both high and low frequencies.

166 *d. Frequency Analysis*

167 The analysis now moves into Fourier space using auto and cross spectra. Complex notation
 168 will be used with Fourier transformed quantities underlined to differentiate them from constants or
 169 functions of time. Since $e^{i(kx - \omega t) + kz}$ is common to all expressions, it will be omitted. For example,
 170 (5) and (6) are now written as a

$$\underline{a}_x = -i \underline{a} \omega^2 \quad (22)$$

$$\underline{a}_z = -\underline{a} \omega^2 \quad (23)$$

172 where \underline{a}_x , \underline{a}_y and \underline{a} are complex numbers and are functions of frequency ω . \underline{a}_x is underlined since
 173 it could be a function of time or frequency. The time derivatives are replaced by multiplication
 174 by $-i\omega$; the derivatives x are replaced by multiplication by ik and the analysis is performed as a
 175 function of ω .

176 Multiple spectral quantities will be computed that combine two arbitrary variables q and r .

- 177 • Spectrum- $\underline{q}\underline{q}^*$ is the magnitude of \underline{q} and is indicated as S_q . \underline{q}^* is the complex conjugate of \underline{q} .
- 178 • Crossspectrum- $C_{qr} = \underline{q}\underline{r}^*$ is the cross-spectrum between \underline{q} and \underline{r} .
- 179 • Coherence- $Coh_{qr} = C_{qr}/(S_q S_r)^{0.5}$ is the coherence between \underline{q} and \underline{r} .
- 180 • Transfer spectrum- $T_{qr} = Coh_{qr}/S_r$ is the transfer spectrum to \underline{q} from \underline{r} .

181 As written above, S and C have units of variance or covariance. They must additionally be
 182 normalized by a spectral bandwidth to be cast into the usual spectral units of variance/bandwidth.
 183 Coh and T are dimensionless and must be cast into the usual units of 1/bandwidth.

184 The notation is further simplified by using the following subscripts:

- 185 • A for Θ_A for horizontal Acceleration (17)
- 186 • Z for Φ_Z for Z acceleration (18).
- 187 • G for Θ_G for effective gravity vector (10).
- 188 • Y for Θ_Y for gYros (21)
- 189 • I for Θ_I for Inertial, computed internally by AHRS

190 Thus, the transfer spectrum to $\underline{\Theta}_I$ from $\underline{\Theta}_G$ is T_{IG} ; to $\underline{\Theta}_I$ from $\underline{\Phi}_Z$ is T_{IZ}

191 *e. Combining Float and Wave Dynamics and Kinematics*

192 We assume that the float's acceleration is the same as the water's acceleration

$$\underline{A}_z = \underline{a}_z \quad (24)$$

$$\underline{A}_x = \underline{a}_x. \quad (25)$$

193 Combining (22) and (23) with (25) yields

$$\underline{A}_x = i\underline{A}_z; \quad (26)$$

194 horizontal and vertical accelerations have the same magnitude, but are 90° out of phase since the
 195 water parcel trajectories are circles. Inserting this into (9), expresses the variations in effective
 196 gravity in terms of the measured Z acceleration (16)

$$\underline{\Theta}_G = \underline{a}_x/g = \underline{A}_x/g = i\widehat{\underline{A}}_z/g. \quad (27)$$

197 Putting (27) back into (17) yields

$$\underline{\Theta}_W = (\underline{\Theta}_A + \underline{\Theta}_G) / (1 + \frac{\omega^2}{\omega_L^2}). \quad (28)$$

198 where $\underline{\Theta}_W$ is a ‘‘Wave’’ estimate of θ computed from the accelerometer data. This combination is
 199 possible due to the combined constraints imposed by float dynamics (25) and wave dynamics (26)
 200 and will not necessarily apply to other types of platform.

201 *f. Consistency tests*

202 $\underline{\Theta}_W$ and $\underline{\Theta}_Y$ are independent measurements of wave tilt. We can therefore test the accuracy
 203 of our analysis assumptions by comparing their autospectra, transfer functions, and coherences.
 204 Multiplying each side of (28) by $\underline{\Theta}_Y^*$ and dividing by $\underline{\Theta}_Y \underline{\Theta}_Y^*$, forms the transfer function

$$T_{WY} = (T_{AY} + T_{GY}) / (1 + \frac{\omega^2}{\omega_L^2}). \quad (29)$$

205 Multiplying (28) by $\underline{\Theta}_W^*$, i.e. finding its squared magnitude, gives the spectrum of $\underline{\Theta}_W$

$$S_W = [S_A + S_G + 2 \Re(C_{AG})] / (1 + \frac{\omega^2}{\omega_L^2})^2 \quad (30)$$

206 where \Re is the real part. A normalized spectra difference between S_W and S_Y is

$$\Delta S_{WY} = 2 \frac{S_W - S_Y}{S_W + S_Y}. \quad (31)$$

207 If $T_{WY} = 1$ and $\Delta S_{WY} = 0$, then the measurements are consistent with the assumptions of the analysis,
 208 i.e. two-dimensionality, linear wave dynamics, small angles and known float geometry. Deviations
 209 from this imply that one or more of these assumptions are imperfect.

210 Similarly, multiplying each side of (28) by $\underline{\Theta}_I^*$ and dividing by $\underline{\Theta}_I \underline{\Theta}_I^*$,

$$T_{WI} = (T_{AI} + T_{GI}) / (1 + \frac{\omega^2}{\omega_L^2}). \quad (32)$$

211 A normalized spectral difference between S_W and S_I is

$$\Delta S_{WI} = 2 \frac{S_W - S_I}{S_W + S_I} \quad (33)$$

212 If $T_{WI} = 1$ and $\Delta S_{WI} = 0$ then the value of tilt computed internally by the AHRS is consistent with
213 the assumptions of the analysis.

214 4. Ocean Measurements



215 FIG. 3. Lagrangian float with a Nortek Signature ADCP and two CTDs. Inset shows a slightly different model
216 of the float with the drogue open. The float displaces about 53 L and is 1.4 m long between the two CTDs; the
217 main tube is 254 mm in diameter.

218 *a. Setting*

219 Measurements were made as part of two Departmental Research Initiatives of the Office of Naval
220 Research: Waves, Langmuir Cells, and the Upper Ocean Boundary Layer (LCDRI) and Coherent
221 Lagrangian Pathways from the Surface Ocean to Interior (CALYPSO). LCDRI measurements
222 were made during March and April 2017 between Catalina and San Nicolas Island off the coast of
223 southern California (Ma et al. 2020). During the 17 days of operation, the wind varied from nearly
224 calm to 18 m/s, producing a wide range of wind and wave conditions, resulting in four major mixing
225 events producing mixed layers up to 30 m deep. Between these, the ocean restratified to form very
226 shallow and diurnally varying mixed layers (Zeiden et al. 2024). CALYPSO measurements were
227 made during April 2019 in the Mediterranean Sea south of Spain (Mahadevan et al. 2020).

228 *b. Surface Waves*

229 During LCDRI, surface waves were measured by at Datawell Waverider buoy at CDIP station
230 229 (<https://cdip.ucsd.edu/themes/cdip/?d2=p70:s:229>) about 70 km west of the operations area
231 and just north of San Nicholas Island and by 8 SWIFT drifters (Thomson et al. 2019) of two
232 different generations at the experimental site. Ma et al. (2020) describes these measurements in
233 detail and compares the different measurements. No significant bias in wave spectra or direction
234 between datasets was found.

235 *c. Lagrangian Float, ADCP and AHRS*

236 Measurements were made using a Lagrangian float (Fig. 3), a versatile platform for upper ocean
237 observations developed and built at the Applied Physics Laboratory of the University of Washington
238 (D'Asaro 2003; D'Asaro et al. 2014; Shcherbina et al. 2019; Alkire et al. 2012). Here, we used data
239 from Lagrangian float 83 (ADCP serial number 100455) deployed in LCDRI and float 82 (ADCP
240 100282) in CALYPSO on multiple missions lasting 1-2 days. During the LCDRI deployments,
241 the float repeatedly profiled from the surface to 30-50 m at about 0.03 m s^{-1} , typically executing
242 36 profiles per day of operation. During CALYPSO it followed water parcels within the mixed
243 layer as they repeatedly cycled across the 30-50 m deep mixed layer. Unless otherwise specified,
244 all data shown are from LCDRI.

245 The float carried a 1 MHz Nortek Signature ADCP (Acoustic Doppler Current Profiler), which
246 included an Inertial Labs OS3DM attitude and heading reference system (AHRS). The ADCP was
247 mounted at a distance L above the float's center of rotation (Fig. 2) and offset to the side. The
248 center of rotation is not easily measured, so L will be estimated from the AHRS data. The AHRS
249 measures the acceleration, rotation rate (rate gyros), and magnetic field vectors and computes the
250 float orientation from these using a proprietary algorithm.

251 5. Analysis and Results

252 *a. Data selection and processing*

253 The analyses in Sections 2 and 3 assume that the surface waves are two-dimensional, with small
254 tilts, and that the float does not rotate around the z axis and only tilts around the y axis. For real
255 data, this is clearly wrong. We selected and pre-processed the float data to minimize these effects.

256 First, the acceleration and rotation rate vectors were rotated around the \hat{z} axis to a coordinate
257 frame with the x -axis aligned down-wave using the wave direction computed by the CDIP buoy at
258 a frequency of 0.3 Hz and a floating head from the AHRS corrected for magnetic declination and
259 hard iron effects. Second, only data from the upward profiles were used, since during downward
260 profiles the float typically rotated $30^\circ - 60^\circ$ in a 15 second wave period, enough to invalidate the
261 two-dimensional assumption. Rotation during upward profiles is about $\pm 7.5^\circ$ in 15 seconds as the
262 drogue stays close to the float hull. Finally, the depth range analyzed was chosen to have small float
263 tilt angles; a depth range of 10-20 m has typical rms tilts during storms of 0.7° but with 99% of
264 the tilts less than 4° (SM, Section 1). Spectral estimates were computed for upward profiling data
265 segments with mean pressures of 10-20 dbar, including only segments with at least 1024 points,
266 and between 5 and 20 m long. FFT's were 512 point long, 50% overlapped with half-cosine (Hann)
267 windows. Auto- and cross-spectra were calculated from the average of all segments in each of the
268 deployments.

269 *b. Data limitations*

270 Our analyses assume that the float is much smaller than the surface wave scales. In reality, the
271 float size L_f becomes comparable to the inverse wavenumber of the surface wave (wavelength/ 2π)
272 when $kL_f = 1$, which occurs at about 0.4 Hz for $L_f=1.3$ m. At higher frequencies, the float

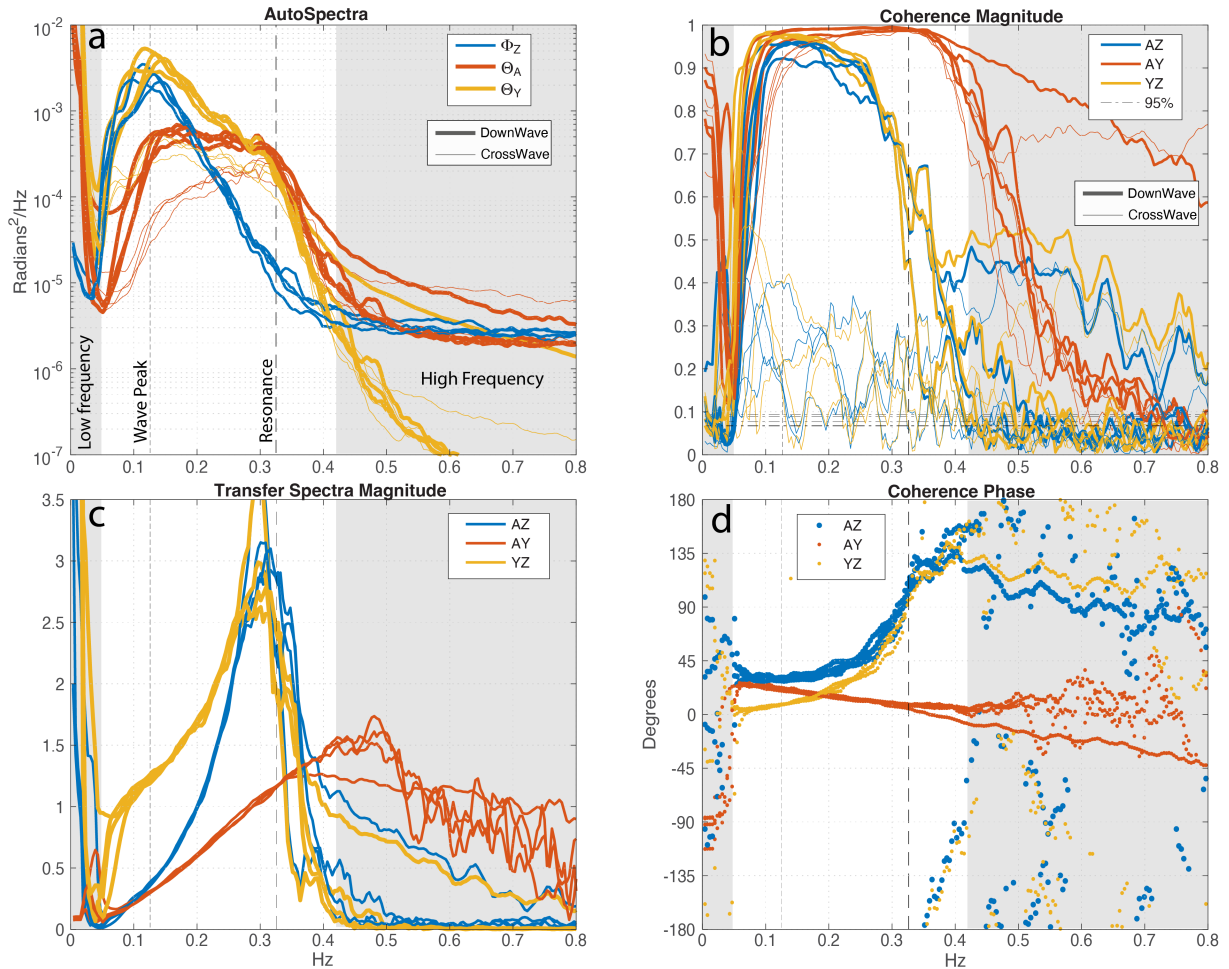
273 spatially averages the wave properties (Lien et al. 1998) and can no longer accurately follow
274 the wave accelerations. D’Asaro (2015) describes corrections for this effect, but these are not
275 implemented here. Our analyses will therefore not apply above a frequency of about 0.4 Hz.

276 Our analyses assume that the surface wave field is two-dimensional. In reality, the waves have
277 a broad directional spectrum propagating mostly downwind, which should produce cross-wind
278 tilts. Indeed, the data shows that Ω_x has magnitudes similar to Ω_y at surface wave frequencies.
279 Furthermore, Ω_z fluctuations have similar magnitudes. This is unexpected since the waves are
280 irrotational, but probably results from the vertical gradient in surface wave velocity acting on the
281 asymmetrical drag of the float due to the ADCP. Both of these effects will introduce noise into the
282 down-wave component, We will address the importance of this using the consistency tests (Section
283 3d).

284 *c. Observed Spectra*

285 Figure 4 shows spectra for 4 deployments selected to have large surface wave signals. The peak
286 surface wave frequency ($\sim 0.12\text{Hz}$) and the resonant frequency of the float ($\sim 0.3\text{ Hz}$; see Section
287 6) are marked by dashed vertical lines. The analysis is carried out over a frequency range starting
288 at the lowest wave frequency ($\sim 0.05\text{ Hz}$) and ending where the finite size of the float significantly
289 attenuates the wave signal ($\sim 0.45\text{ Hz}$). Regions outside of this band are shaded.

290 The autospectra (Fig. 4a) of vertical acceleration Φ_Z (blue thick) rise rapidly to the peak wave
291 frequency and then fall to a white noise floor outside the wave band. In contrast, the autospectra
292 of the tilt from horizontal acceleration Θ_A (red thick) rise to a plateau at the wave peak and remain
293 nearly constant to the resonance frequency, before falling to the same noise floor. The autospectra
294 of tilt from rotation rate Θ_Y (orange thick) rise to the wave peak, decay more slowly to the resonance
295 frequency, and then fall rapidly to levels far below the accelerometer noise floor. The coherence
296 magnitude between Θ_A and Θ_Y (Fig. 4b, thick red, AY) is nearly 1 in the wave band, while the
297 phase (Fig. 4d) decreases linearly by about 45° . The coherence magnitudes of Θ_A or Θ_Y with
298 Φ_Z (AZ-blue and AY-orange) are high at the frequency of the wave peak, but fall rapidly through
299 the resonance frequency to nearly zero values above the wave band, while their phase increases
300 by about 90° across the wave band. The transfer spectra (Fig. 4c) have a strong peak close to the
301 resonant frequency for all quantities. Overall, the spectra suggest a resonant response near 0.3 Hz.



302 FIG. 4. Tilt spectra from 4 selected float 83 LCDRI deployments with large wave signals. The different
 303 realizations provide an estimate of the variability. Data is rotated into down-wave (thick lines) and cross-wave
 304 (thin lines) directions. Tilts are computed from different sources: 'A', horizontal acceleration, 'Z' vertical
 305 acceleration, and 'Y', integrated rotation rate. Vertical dashed lines indicate float resonance frequency and
 306 approximate wave peak. Shading denotes frequencies below the surface wave band, where the wave dynamics
 307 analyzed here does not apply, and above about 0.4 Hz, where noise and finite float size begins to dominate the
 308 measurements. a) Autospectra for downwave and crosswave tilts. b) Coherence magnitude between different tilt
 309 measurements labeled so that 'QR' is transfer from source Q to source R. Horizontal dashed lines shows 95%
 310 levels of no significance. c) Transfer function magnitudes. d) Phase for transfer function and coherence.

311 The thin lines in Fig. 4ab show the same spectra for the cross-wave components. The autospectra
 312 are somewhat smaller, but the coherences are much smaller, so the phase is noisy and not shown.
 313 Perhaps the contributions of waves to the right and left of the down-wave direction cancel. Re-

314 gardless, the analysis framework does not include these waves, and with little coherence or theory
315 we cannot analyze them further.

316 *d. Consistency Tests: Analysis, sensor and AHRS errors*

317 1) ROTATION AND ACCELEROMETER MEASUREMENTS

318 Fig. 5 evaluates the consistency tests for the down-wave data in Fig. 4 for frequencies within the
319 surface wave band. The coherences AZ, AY and YZ (Fig. 5b) are high throughout the band. In
320 general Θ_W and Θ_Y are close to consistent. The ΔS_{WY} is about 0.08. The imaginary part of T_{WY}
321 is zero within the uncertainty of the four realizations (Fig. 5 d). $\Re(T_{WY})$ is about 3% above 1.0
322 (Fig. 5c). The remaining inconsistency in ΔS_{WY} and $\Re(T_{WY})$ could be corrected by increasing the
323 magnitude of $\underline{\Theta}_Y$ by 3.5% (Fig.5ac, thin red lines).

324 The value of L is determined from the consistency tests. Varying L adds an upward or downward
325 curvature to $\Re(T_{WY})$ and ΔS_{WY} . For example, using a value of $L = 0.4\text{m}$ causes $\Re(T_{WY})$ to bend
326 downward, reaching 1.0 at about 0.33 Hz. We use $L = 0.3\text{ m}$ with an estimated accuracy of 0.05 m.

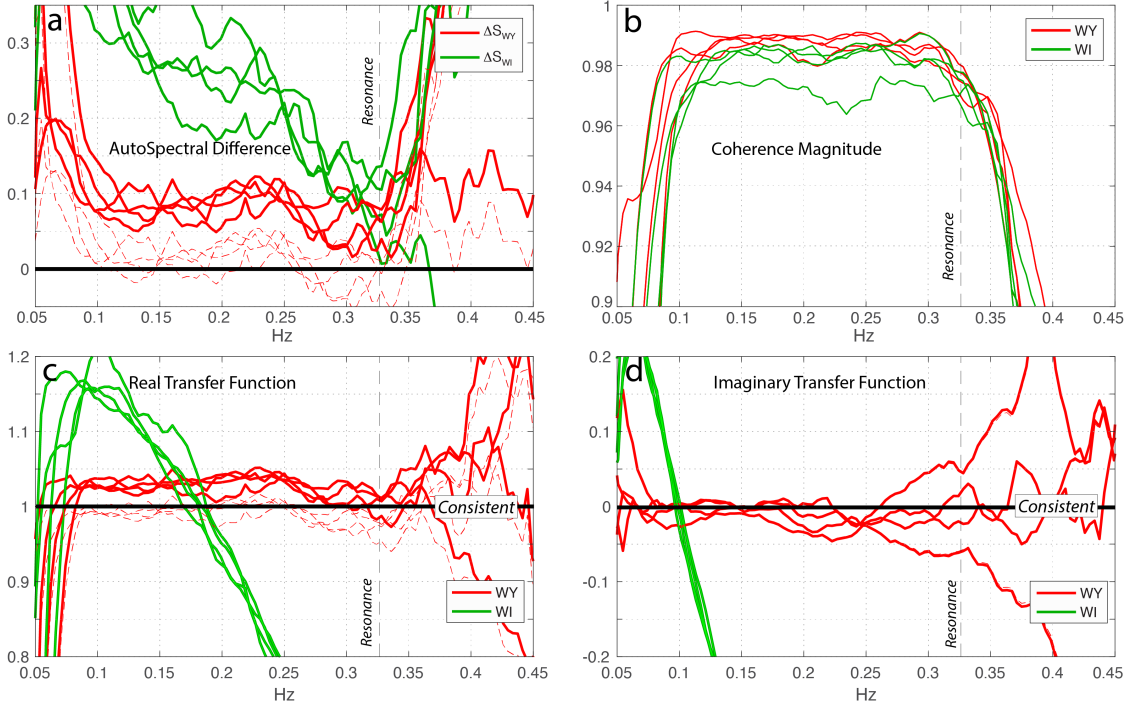
327 Θ_W , Θ_A and Θ_Y were also compared in the laboratory by swinging the AHRS on a variety of
328 pendulums (SM Section 3). The Θ_Y and a Θ_W modified for the laboratory geometry were consistent
329 to a few percent and Θ_Y had a noise level within the surface wave band of a fraction of a degree.

330 Overall, these results indicate that the combination of careful data selection, rotation in the
331 down-wave direction, and selection of a limited range of frequencies has limited the combined
332 errors from the measurements and in the assumptions of two-dimensionality, linearity and small
333 angles to about 3%. It is surprising that they are this small.

334 2) AHRS TILTS

335 In contrast, Θ_W and Θ_I are not consistent. The real and imaginary parts of T_{WI} and ΔS_{WI} (green
336 lines) are much further away from the consistent values (black horizontal lines) than could be due
337 to measurement or sampling uncertainty. We expect Θ_A to accurately measure small tilts at low
338 frequency (17) and use this to test the accuracy of Θ_I under these conditions (SM, Fig. S1b).
339 They agree better than 0.1° . Similarly, we expect Θ_Y to accurately measure the tilts in the surface
340 wave frequency band. This is true to about 0.1° when the tilts are small (SM, Fig. S1c), but not
341 when they are large (SM, Fig. S1d). In laboratory tests, Θ_W and Θ_I are nearly consistent at small

342 tilts. However, for large tilts, both in field and laboratory data, Θ_I can episodically have large
 343 errors. These results suggest that the AHRS tilts are only reliable for small tilts and suggest some
 344 systematic errors even for small tilts. A detailed diagnosis is beyond the scope of this paper.



345 FIG. 5. Consistency tests for spectra in Fig. 4. Each panel shows consistency tests for 4 float deployments:
 346 red for WY tests between Θ_W and Θ_Y , and green for WI tests between Θ_W and Θ_I . The results for perfect
 347 consistency are indicated by the horizontal black lines. The solid lines show results for the data; the thin dashed
 348 lines show results of increasing the gain on the rate gyros by 3.5%. a) Normalized autospectral difference (31)
 349 and (33), b) coherence magnitude, Θ_W to Θ_Y (red) and Θ_W to Θ_I (green). c) Real part of transfer function, Θ_W
 350 to Θ_Y and Θ_W to Θ_I , equations (29) and (32). d) Same but for imaginary part of transfer function.

351 6. Float Response Model

352 a. Dynamics

353 We wish to predict the displacement and tilt of a subsurface float in a surface wave field.
 354 The analyses in D'Asaro (2015) and the consistency tests above indicate that the acceleration of
 355 Lagrangian floats, and thus their displacement, match that of the water at surface wave frequencies
 356 to within the accuracy of the measurements and thus can be modeled by (1)-(6). No additional

357 modeling is needed, although corrections for the finite size of the float (D’Asaro 2015) might be
 358 required.

359 The tilt of the float is governed by a balance of hydrostatic and hydrodynamic torques. The
 360 hydrostatic torque arises from the righting moment because of the buoyancy and mass distribution
 361 of the float. The hydrodynamic torque results from the interaction between the float’s geometry
 362 and the strain field of the ambient flow, and can induce rotation even when the surrounding flow is
 363 irrotational. In steady irrotational flows, rigid elongated bodies rotate to orient themselves in the
 364 principal direction of strain (e.g., Junk and Illner 2007), as follows from the classic Jeffery’s theory
 365 (Jeffery 1922). In the case of a time-varying strain field associated with surface gravity waves, the
 366 alignment kinematics are generally nonlinear (Ma et al. 2022). In our case of an initially vertical
 367 body and under the small-angle approximation, strain-aligned angle can be approximated to first
 368 order as

$$\theta_J = -\alpha k \lambda e^{kz} \sin(kx - \omega t) = \lambda \theta_Z, \quad (34)$$

369 where subscript "J" stands for Jeffery’s alignment angle (cf. eq.13c of Ma et al. (2022)). The
 370 shape eccentricity parameter $\lambda \in [-1, 1]$ is defined as $\lambda = (L_{\parallel}^2 - L_{\perp}^2) / (L_{\parallel}^2 + L_{\perp}^2)$, where L_{\parallel} and L_{\perp}
 371 are the diameters parallel and perpendicular to the main axis of symmetry of a body¹; it describes
 372 the range of shapes from a flat disk ($L_{\parallel} \ll L_{\perp}$, $\lambda = -1$) to a thin rod ($L_{\parallel} \gg L_{\perp}$, $\lambda = 1$).

373 Equation (34) supports the intuitive notion that, in absence of a righting moment, a thin initially
 374 vertical rod would orient itself along the Z-lines ($\lambda = 1 \rightarrow \theta_J = \theta_Z$), while a flat disc would tilt in
 375 the opposite direction ($\lambda = -1 \rightarrow \theta_J = -\theta_Z = \theta_G$) and orient itself with the P-lines (so that its axis
 376 is aligned with the effective gravity vector \vec{g}_e). These two limiting cases of wave-induced tilting
 377 correspond to the "inertial" and "hydrostatic" response modes, respectively (Longuet-Higgins
 378 1986). A generically shaped body can be expected to have an intermediate alignment angle
 379 described by (34), as discussed by Shcherbina and D’Asaro (2025).

380 The hydrostatic righting torque always acts to align the float’s axis with the effective gravity
 381 vector \vec{g}_e . Thus, it enhances hydrostatic tilting ($\lambda < 0$) but opposes the inertial response ($\lambda > 0$).
 382 A general dynamic model of the float’s tilt should therefore include terms accounting for both the
 383 hydrodynamic (strain alignment) and hydrostatic (righting moment) torques. Theoretical modeling

¹Even though the original Jeffery (1922) theory was developed for ellipsoid bodies, Bretherton (1962) later demonstrated that it applies to any rotationally-symmetric shape. In such general cases, the parameter λ is interpreted as an effective eccentricity parameter, although its definition is not as straightforward as in the ellipsoidal case.

384 of these combined effects is challenging due to several factors, including the irregular shape of the
 385 float, its finite size, and the potential for turbulent flow. We therefore adopt an empirical approach,
 386 guided by observed behavior and the considerations outlined above.

387 *b. Model formulation*

388 We adopt an empirical model for the float's tilt in the $x\tilde{z}$ plane, governed by the balance between
 389 the righting torque and the strain-alignment torque:

$$\frac{d^2\theta}{dt^2} = -\sigma^2(\theta - \theta_G) - r\frac{d}{dt}(\theta - \theta_J). \quad (35)$$

390 The left-hand side represents the change in the angular momentum of the float, i.e. the angular
 391 acceleration. The rotational moment of inertia (including any added mass effects) is divided out
 392 and absorbed by the right-hand side coefficients. The right-hand side is the sum of the torques
 393 discussed in Section 6a, parameterized by empirical linear coefficients. The first term on the right
 394 parameterizes the angular acceleration of the float towards the direction of effective gravity θ_G
 395 (10) using the rate parameter σ^2 . By itself, this term results in a harmonic oscillation of $\theta - \theta_G$ at
 396 frequency σ .

397 The second term linearly parameterizes the torque due to the misalignment of the float and the
 398 wave strain field; it vanishes when the float orientation matches the Jeffery's angle $\theta_J = \lambda\theta_Z = -\lambda\theta_G$.
 399 The coefficient r is the ratio between the rotational drag and the rotational moment of inertia of the
 400 float. By itself, this term results in an exponential decay of $\theta - \theta_J$ at a rate r . The Jeffery theory
 401 underlying this term applies to an infinitesimal particle in a low-Reynolds-number Stokes flow,
 402 quite different from that of a finite-sized float in a turbulent boundary layer. An empirical approach
 403 to that environment might invoke frictional torques resulting from the asymmetry of the body in
 404 the time-dependent wave strain field as $\alpha\frac{d}{dt}(\theta - \theta_Z) + \beta\frac{d}{dt}(\theta - \theta_P)$ where α and β parameterize the
 405 drag from the motion of the oppositely tilting Z and P lines. This yields an equation identical to
 406 (35), suggesting that this term is a general linear parameterization of the interaction between wave
 407 strain and the float asymmetry.

408 Using (34) and (12), we can rewrite the float tilt model (35) as a linear, damped harmonic
 409 oscillator driven by the forcing angle θ_G :

$$\frac{d^2\theta}{dt^2} = -\sigma^2(\theta - \theta_G) - r\frac{d}{dt}(\theta + \lambda\theta_G). \quad (36)$$

410 OR

$$\frac{d^2\theta}{dt^2} + r\frac{d\theta}{dt} + \sigma^2\theta = \sigma^2\theta_G + \gamma\frac{d\theta_G}{dt}, \quad (37)$$

411 where $\gamma = -\lambda r$. If the float had no righting moment ($\sigma = 0$) and no shape eccentricity ($\lambda = \gamma = 0$),
 412 it would not tilt. Rotational drag alone ($r > 0$) does not cause tilt, since the flow field is irrotational;
 413 either eccentricity or a righting moment are required. Coefficients σ , r , and γ have dimensions of
 414 inverse time and units of $rad\ s^{-1}$, abbreviated as s^{-1} . They are to be determined empirically.

415 Estimation of the model coefficients is most effectively performed in Fourier space (see section
 416 3b), where (37) becomes

$$-\omega^2\underline{\theta} - i\omega r\underline{\theta} + \sigma^2\underline{\theta} = \sigma^2\underline{\theta}_G - i\omega\gamma\underline{\theta}_G. \quad (38)$$

417 This corresponds to a transfer function $T_{\theta G}$ from the wave forcing $\underline{\theta}_G$ to the tilt $\underline{\theta}$ of the float

$$T_{\theta G} = \frac{\sigma^2 - i\gamma\omega}{\sigma^2 - \omega^2 - ir\omega} = -\frac{\sigma^2 - i\gamma\omega}{(\omega - \sigma_{r+})(\omega - \sigma_{r-})} \quad (39)$$

418 with the roots of the denominator

$$\sigma_{r\pm} = \sigma(\pm[1 - Q^{-2}]^{0.5} - i/Q) \quad (40)$$

419 and

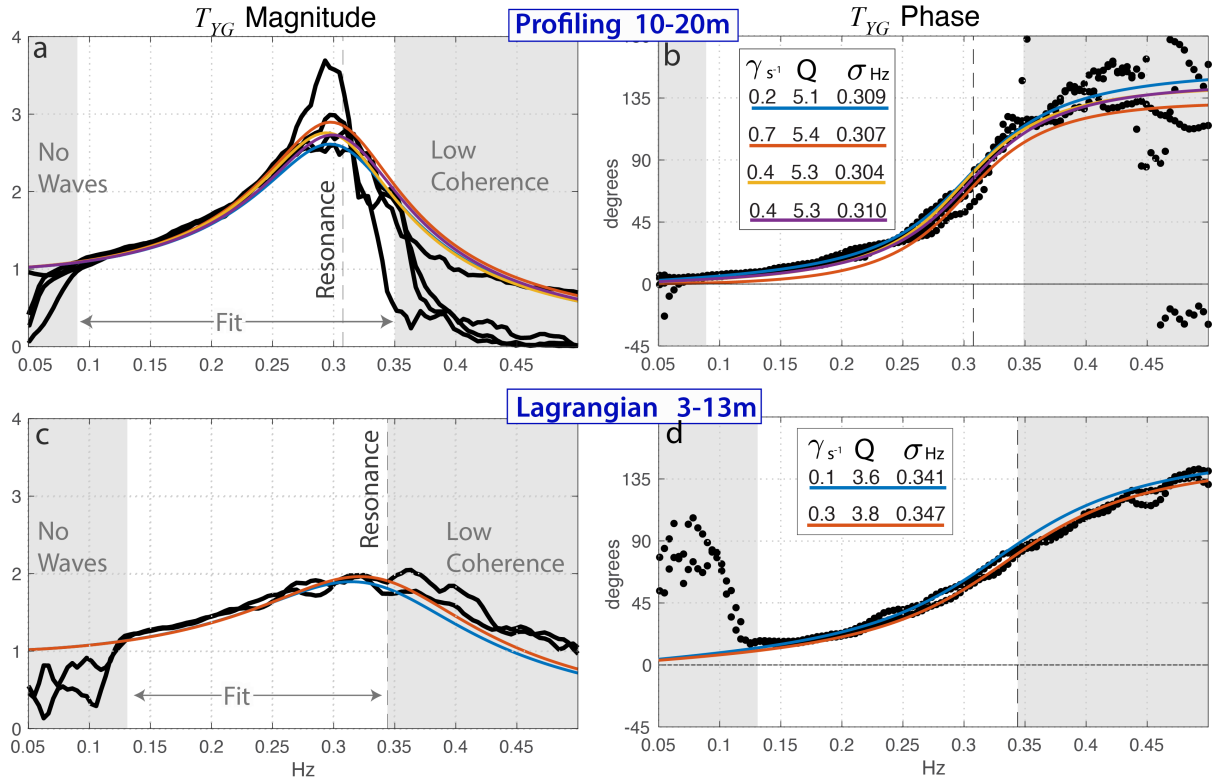
$$Q = 2\sigma/r \quad (41)$$

420 This is a resonant system with 3 independent parameters: a resonant frequency σ , a quality
 421 factor Q , and an asymmetry parameter γ . One might expect this system to be characterized by
 422 four parameters specifying the resonance frequency, the damping rate, and the forcing amplitude
 423 in terms of θ_G and $d\theta_G/dt$. Our formulation uses only 3, since σ^2 specifies both the resonant
 424 frequency and the forcing by θ_G .

425 *c. Model evaluation*

426 The model response $T_{\theta G}$ will be evaluated using Θ_G from (27) and $\underline{\theta}$ from $\underline{\Theta}_Y$ because it has
 427 lower noise and a higher signal than $\underline{\Theta}_A$ and does not require the estimation of L . Using (39), the
 428 float response model is thus

$$T_{YG} = \frac{\sigma^2 - i\gamma\omega}{\sigma^2 - \omega^2 - ir\omega} \quad (42)$$



429 FIG. 6. (a) Magnitude and (b) phase of T_{YG} (42) for data segments in Fig. 4. The same quantities for the
 430 CALYPSO data are shown in (c-d). Colored lines are least squares model fit over the white frequency domain.
 431 The shaded regions not used for fitting vary between the two deployments due to differences in the peak wave
 432 frequency and coherence. Model parameters for each fit are listed in the box.

433 Figure 6 shows the fits of the model to the data. The parameters were found by minimizing the
 434 summed squared difference between the prediction of the model of T_{YG} and the data, both real and
 435 imaginary parts. The fitting was performed over a frequency range of 0.09-0.35 Hz, between the
 436 lowest frequency of the surface waves and the frequency at which the gyro- and vertical acceleration
 437 measurements become incoherent (Fig. 4). The fittings were performed separately for each float

Float Model Parameters

	Mean \pm Variation			
$\frac{\sigma}{2\pi}$	0.32	$\pm 7\%$		Hz
σ	2.01	$\pm 7\%$		$rad\ s^{-1}$
Q	4.75	$\pm 19\%$		
r	0.88	$\pm 27\%$		s^{-1}
γ	0.37	$\pm 82\%$		s^{-1}
λ	-0.47	$\pm 95\%$		

TABLE 1. Mean values of the model parameters for the 6 model fits in Fig 6. Variation is given as half of the maximum - minimum parameter value as a percentage of the mean.

deployment with the variation between deployments used to assess the variability in the parameters. The same 4 cases as in Fig. 4 are shown.

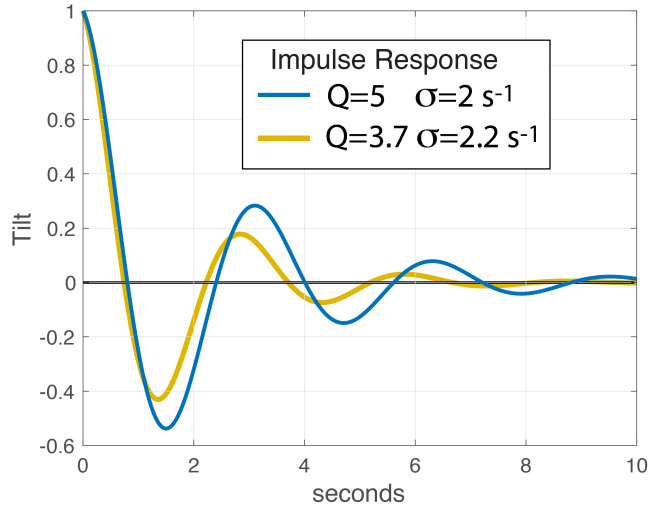
At the resonant peak, the data (black) show a maximum amplitude (Fig. 6a) and a rapid phase change (Fig. 6b). The model (colored lines) fits both features well, but with decreasing accuracy for frequencies greater than σ due to decreasing coherence. The mean rms deviation of the model from the data is about 10%, 0.2 out of a typical signal of 2.

For comparison, the same analysis was performed on about 38 hours of data from a Lagrangian float deployed during the 2019 CALYPSO experiment (Mahadevan et al. 2020) under strong wind forcing ($\sim 11\ m\ s^{-1}$) and relatively short fetch. Unlike the LCDRI float, which profiled with a partially folded drogue and was sometimes in the mixed layer and sometimes beneath it, this float operated in a Lagrangian mode with the drogue open and thus followed the three-dimensional motion of the water, repeatedly crossing the 30-50 m deep mixed layer. Spectra of the float motion are similar to those for the LCDRI float, but model fits (Fig. 6cd) yield a slightly higher resonant frequency, and smaller values of Q . A similar increase in σ and a decrease in Q is found for 2 low-wave data segments from LCDRI.

Table 1 lists the parameter fits for the 6 data segments plotted in Fig. 6.

d. Implications

The values of the derived parameters are reasonable. The resonant frequency σ is equivalent to that of a simple pendulum $L = 0.4\ m$ long, approximately 30% of the float length. The values of $Q = 5$ ($r = 0.6\ s^{-1}$) for LCDRI and $Q = 3.7$ ($r = 1.2\ s^{-1}$) for CALYPSO are consistent with a



456 FIG. 7. Impulse response of the float model. Units are normalized to 1 at time=0. Blue: $Q = 5$ and
 457 $\sigma = 2 \text{ rad s}^{-1}$, orange: $Q = 3.7$ and $\sigma = 2.2 \text{ rad s}^{-1}$

462 larger rotational drag in CALYPSO, since the drogue was open. For both, the model implies that
 463 the float is somewhat underdamped and will exhibit a decaying oscillation of a few cycles when
 464 perturbed (Figure 7). Visual observations of the float when it is on the surface qualitatively show
 465 this behavior. For LCDRI, $\gamma = 0.45 \text{ s}^{-1}$ and $\lambda = -0.6$, implying a mostly hydrostatic response. The
 466 negative sign of the eccentricity parameter λ is surprising, as it corresponds to an equivalent
 467 oblate ellipsoid with $L_{\parallel} : L_{\perp} = 1 : 2$, in stark contrast to the actual prolate geometry of the float's
 468 hull ($L_{\parallel} : L_{\perp} \approx 5 : 1$). The CALYPSO response shows weaker strain alignment and eccentricity
 469 parameter closer to zero ($\lambda = -0.2$). This value, by itself, appears to be consistent with a more
 470 symmetric shape of the float when its drogue is open. However, the decrease in λ in LCDRI
 471 could be due to the closed drogue decreasing L_{\perp} or due to the much larger mean flow past the
 472 float, roughly 0.1 m s^{-1} in LCDRI compared to less than 0.01 m s^{-1} , in CAYPSO. Furthermore, the
 473 wide range of variability in the best-fit values of λ (ranging from -0.98 to -0.1) suggests that this
 474 parameter is poorly constrained by the data or, equivalently, that this parameter has only a small
 475 influence on the response function.

476 7. Summary

477 Subsurface and nearly neutrally buoyant floats can be stable and well behaved platforms for
 478 measuring ocean dynamics in the near-surface wave zone. Here, we investigate and model their

479 motion and tilts. A future paper will model the resulting errors in ADCP measurements following
480 Shcherbina and D’Asaro (2025).

481 A Nortek Signature 1000 ADCP with AHRS (Attitude and Heading Reference System) on a
482 Lagrangian float deployed in the upper ocean in a variety of wind and wave conditions measured
483 the acceleration, magnetic field, and rotation rate of the float. The same AHRS was tested in the
484 laboratory by swinging it on a variety of pendulums with frequencies similar to those of surface
485 waves. We used these data to test the accuracy of various estimates of the float tilt and to generate
486 a model to predict these tilts from surface wave properties as follows:

- 487 • Float tilts are assumed to be small, confined to a plane, and driven by linear surface waves.
488 The float is assumed to move with the surface waves.
- 489 • Data records are chosen so the tilts are small and the rotation rates around the vertical axis are
490 small enough to be unimportant at surface wave frequencies. Data are rotated, so the analysis
491 plane is aligned downwave. The analyses are conducted in a frequency band between the
492 lowest surface wave frequency and the highest frequency, where the finite float size effects are
493 small.
- 494 • The vertical displacements of surface waves are measured from vertical acceleration. Float tilt
495 θ is estimated in three redundant ways: measured rotation rates are integrated to compute Θ_Y .
496 Surface wave dynamics are used to merge vertical and horizontal acceleration and compute
497 Θ_W . The AHRS computes Θ_I using a proprietary algorithm.
- 498 • Comparison of these 3 tilt estimates is used to test the accuracy of the measurements, the
499 analysis assumptions and the AHRS algorithm in both the field data and laboratory tests
500 finding:
 - 501 – Θ_Y has a noise level low enough to provide accurate measurements of the tilt variations
502 within the surface wave band to a fraction of a degree.
 - 503 – Θ_Y and Θ_W are consistent with the assumptions to about 3%, a surprisingly small number.
 - 504 – Θ_I is only reliable for small tilts and has clear errors for tilts larger than a few degrees.
- 505 • Float tilt is empirically modeled as a linear damped harmonic oscillator driven by linear surface
506 waves. The model has 3 parameters, physically corresponding to the float’s righting moment,

507 rotational drag, and shape eccentricity. These yield the resonant frequency, the quality factor
508 Q , and the asymmetry of the coupling to the periodic wave strain field. Since the float follows
509 the nearly circular oscillating trajectories of water parcels beneath surface waves, the effective
510 direction of gravity felt by the float oscillates at the surface wave frequency. Tilts are forced
511 primarily by the float's righting moment continually seeking this direction. The tilt is also
512 forced by the wave strain interacting with the float's shape.

- 513 • The model fits the data from multiple float deployments under different conditions to an
514 accuracy of about 10%. The resonant period is about 3 seconds and Q is 3 – 6 depending on
515 the float configuration. These Lagrangian floats are thus a somewhat underdamped oscillator
516 and will exhibit a decaying oscillation of a few cycles when perturbed.

517 **8. Discussion**

518 The analysis presented here assumes an idealized float geometry and that the surface waves are
519 two-dimensional and have small slopes. This greatly simplifies the analyses and leads to simple
520 dynamics and remarkably robust results, but limits their generality. Real surface waves have a large
521 directional spread, which can cause float tilts and rotations of similar magnitudes in all directions.
522 Here, a careful choice of data allowed the analysis to minimize these effects and extract and model
523 tilts in the down-wave direction; this is not true under all conditions. However, the results are
524 sufficient to provide a useful tilt response function for understanding the errors in Lagrangian float
525 measurements, specifically the errors in ADCP measurements resulting from float motion in the
526 wave zone.

527 A disturbing result of this study is that general purpose AHRS sensors may at times yield very
528 poor estimates of orientation, far worse than their specifications, even if the underlying sensors are
529 providing accurate data. We found that simple tests using pendulums with periods similar to those
530 of surface waves can help detect such problems. Although the AHRS outputs can exhibit large
531 errors and were inconsistent with the constraints imposed by the float geometry and wave forcing,
532 they agreed well with those computed directly from the sensors for small tilts. Apparently, the
533 generic AHRS algorithm used was accurate enough, despite its imperfections. An algorithm that
534 included the constraints of float geometry and wave forcing might yield more accurate results over
535 a wider range of tilts.

536 The Lagrangian floats characterized here have a resonant frequency within the surface wave
537 band, which amplifies their response to the waves. Since the wave energy decreases rapidly with
538 frequency, float tilting could be significantly decreased if the resonance were moved to higher
539 frequencies. For example, in Fig. 6 the wave forcing at 0.4 Hz is about a factor of 10 less than that
540 at the resonance of 0.31 Hz. Increasing the resonant frequency by this factor of 1.3 would decrease
541 the rms tilt by about a factor of 3. This could be done by increasing the float length by a factor of
542 about 1.7 and keeping other things the same. This might have other undesirable effects, such as
543 making the float more difficult to handle and attenuating its response to high-frequency turbulent
544 signals (Lien et al. 1998).

545 **9. Acknowledgements**

546 This work was supported by the Office of Naval Research Departmental Research Initiatives,
547 RIOT, CALYPSO and Langmuir (N00014-24-1-2720, N00014-18-1-2139, N00014-18-1-2420,
548 N00014-14-1-0666, N00014-17-1-2859), and by NASA S-MODE project, an EVS-3 Investigation
549 awarded under NASA Research Announcement NNH17ZDA001N-EVS3. We thank the officers
550 and crew of the R.V. Sproul and R.V. Pourquoi Pas? and the engineering staff of the Applied
551 Physics Laboratory.

552 **10. Data Availability Statement**

553 Field and laboratory data are available at DOI: 10.5061/dryad.70rxwdc96

554 **References**

- 555 Alkire, M. B., et al., 2012: Estimates of net community production and export using high-
556 resolution, Lagrangian measurements of O_2 , NO_3^- , and POC through the evolution of a spring
557 diatom bloom in the North Atlantic. *Deep Sea Research Part I: Oceanographic Research Papers*,
558 **64**, 157–174, doi:10.1016/j.dsr.2012.01.012.
- 559 Amador, A., S. Jaramillo, and G. Pawlak, 2017: ADCP bias and stokes drift in auv-based velocity
560 measurements. *Journal of Atmospheric and Oceanic Technology*, **34** (9), 2029–2042, doi:10.
561 1175/JTECH-D-16-0182.1.

- 562 Arduin, F., et al., 2019: SKIM, a candidate satellite mission exploring global ocean currents and
563 waves. *Frontiers in Marine Science*, **6**, 209, doi:10.3389/fmars.2019.00209.
- 564 Bretherton, F. P., 1962: The motion of rigid particles in a shear flow at low Reynolds number.
565 *Journal of Fluid Mechanics*, **14** (2), 284–304, doi:10.1017/S002211206200124X.
- 566 Centurioni, L. R., et al., 2019: Global in situ observations of essential climate and ocean variables
567 at the air–sea interface. *Frontiers in Marine Science*, **6**, 419, doi:10.3389/fmars.2019.00419.
- 568 D’Asaro, E., 2015: Surface wave measurements from subsurface floats. *Journal of Atmospheric
569 and Oceanic Technology*, **32** (4), 816–827, doi:10.1175/JTECH-D-14-00180.1.
- 570 D’Asaro, E. and C. McNeil, 2007: Air–sea gas exchange at extreme wind speeds measured by
571 autonomous oceanographic floats. *Journal of Marine Systems*, **66** (1-4), 92–109, doi:10.1016/j.
572 jmarsys.2006.06.007.
- 573 D’Asaro, E. A., 2003: Performance of autonomous Lagrangian floats. *Journal of Atmospheric
574 and Oceanic Technology*, **20** (6), 896–911, doi:10.1175/1520-0426(2003)020<0896:POALF>
575 2.0.CO;2.
- 576 D’Asaro, E. A., J. Thomson, A. Shcherbina, R. Harcourt, M. Cronin, M. Hemer, and B. Fox-
577 Kemper, 2014: Quantifying upper ocean turbulence driven by surface waves. *Geophysical
578 Research Letters*, **41** (1), 102–107, doi:10.1002/2013GL058193.
- 579 D’Asaro, E. A., et al., 2018: Ocean convergence and the dispersion of flotsam. *Proceedings of the
580 National Academy of Sciences*, **115** (6), 1162–1167, doi:10.1073/pnas.1718453115.
- 581 Gould, W. J., 2005: From Swallow floats to Argo - the development of neutrally buoyant floats.
582 *Deep Sea Research Part II: Topical Studies in Oceanography*, **52**, 3-4, 529–543, doi:10.1016/j.
583 dsr2.2004.12.005.
- 584 Jeffery, G. B., 1922: The motion of ellipsoidal particles immersed in a viscous fluid. *Proc. R. Soc.
585 Lond. A*, **102** (715), 161–179, doi:10.1098/rspa.1922.0078.
- 586 Junk, M. and R. Illner, 2007: A new derivation of Jeffery’s equation. *J. Math. Fluid Mech.*, **9**,
587 455–488, doi:10.1007/s00021-005-0208-0.

- 588 Kumar, B. P., E. D’Asaro, M. Ravichandran, et al., 2019: Widespread cooling of the Bay of Bengal
589 by tropical storm Roanu. *Deep Sea Research Part II: Topical Studies in Oceanography*, **168**,
590 104 652, doi:10.1016/j.dsr2.2019.104652.
- 591 Laxague, N., et al., 2018: Observations of near-surface current shear help describe oceanic oil and
592 plastic transport. *Geophysical Research Letters*, **45 (1)**, 245–249, doi:10.1002/2017GL075891.
- 593 Lien, R.-C., E. A. D’Asaro, and G. T. Dairiki, 1998: Lagrangian frequency spectra of vertical
594 velocity and vorticity in high-Reynolds-number oceanic turbulence. *Journal of Fluid Mechanics*,
595 **362 (177)**, 104, doi:10.1017/S0022112098008787.
- 596 Longuet-Higgins, M. S., 1986: Eulerian and Lagrangian aspects of surface waves. *Journal of Fluid*
597 *Mechanics*, **173**, 683–707, doi:10.1017/S0022112086001325.
- 598 Luyten, J. R. and J. Swallow, 1976: Equatorial undercurrents. *Deep Sea Research and Oceano-*
599 *graphic Abstracts*, Elsevier, Vol. 23:10, 999–1001.
- 600 Ma, B., E. D’Asaro, S. TB, and T. J, 2020: LC–DRI field experiment and data calibration report.
601 Technical Report APL-UW TR 2002, Applied Physics Laboratory, University of Washington,
602 1013 NE 40th Str, Seattle, WA USA.
- 603 Ma, K., N. Pujara, and J.-L. Thiffeault, 2022: Reaching for the surface: Spheroidal microswimmers
604 in surface gravity waves. *Phys. Rev. Fluids*, **7**, 014 310, doi:10.1103/PhysRevFluids.7.014310.
- 605 Mahadevan, A., A. Pascual, D. L. Rudnick, S. Ruiz, J. Tintoré, and E. D’Asaro, 2020: Coherent
606 pathways for vertical transport from the surface ocean to interior. *Bulletin of the American*
607 *Meteorological Society*, **101 (11)**, E1996–E2004, doi:10.1175/BAMS-D-19-0305.1.
- 608 Menemenlis, D., J. Campin, P. Heimbach, C. Hill, L. T., A. Nguyen, M. Schodlok, and H. Zhang,
609 2008: Ecco2: High resolution global ocean and sea ice data synthesis. *Mercator Ocean Quarterly*
610 *Newsletter*, **October**, 13–21.
- 611 Phillips, O. M., 1977: *The Dynamics of the Upper Ocean*. 2d ed., Cambridge Univ. Press, Cam-
612 bridge, UK, 344 pp.

613 Pizzo, N., W. Melville, and L. Deike, 2019: Lagrangian transport by nonbreaking and
614 breaking deep-water waves at the ocean surface. *J. Phys.Oceanogr.*, **49** (4), 983–992, doi:
615 10.1175/JPO-D-18-0227.1.

616 Pollard, R., 1973: Interpretation of near-surface current meter observations. *Deep Sea Research and*
617 *Oceanographic Abstracts*, Elsevier, Vol. 20,3, 261–268, doi:10.1016/0011-7471(73)90015-6.

618 Sanford, T. B., R. G. Drever, and J. H. Dunlap, 1978: A velocity profiler based on the principles
619 of geomagnetic induction. *Deep sea research*, **25** (2), 183–210, doi:10.1016/0146-6291(78)
620 90006-1.

621 Shcherbina, A. Y. and E. A. D’Asaro, 2025: Wave-induced biases in ADCP measurements from
622 quasi-lagrangian platforms. *Journal of Atmospheric and Oceanic Technology*, doi:10.1175/
623 JTECH-D-24-0046.1.

624 Shcherbina, A. Y., E. A. D’Asaro, and R. R. Harcourt, 2019: Rain and sun create slippery layers in
625 the Eastern Pacific fresh pool. *Oceanography*, **32** (2), 98–107, doi:10.5670/oceanog.2019.217.

626 Thomson, J., et al., 2019: A new version of the SWIFT platform for waves, currents, and turbulence
627 in the ocean surface layer. *2019 IEEE/OES Twelfth Current, Waves and Turbulence Measurement*
628 *(CWTM)*, IEEE, 1–7, doi:10.1109/CWTM43797.2019.8955299.

629 Torres, H., A. Wineteer, P. Klein, T. Lee, J. Wang, E. Rodriguez, D. Menemenlis, and H. Zhang,
630 2023: Anticipated capabilities of the ODYSEA wind and current mission concept to estimate
631 wind work at the air–sea interface. *Remote Sensing*, **15** (13), 3337, doi:10.3390/rs15133337.

632 Wenstrand, D. C., 1979: Measurements of vertical profiles of oceanic current and Richardson
633 number near St. Croix, USVI. *Journal of Hydronautics*, **13** (3), 69–76, doi:10.2514/3.48168.

634 Wineteer, A., et al., 2020: Measuring winds and currents with Ka-band doppler scatterometry: An
635 airborne implementation and progress towards a spaceborne mission. *Remote Sensing*, **12** (6),
636 1021, doi:10.3390/rs12061021.

637 Zeiden, K., J. Thomson, A. Shcherbina, and E. D’Asaro, 2024: Observations of elevated mixing
638 and periodic structures within diurnal warm layers. *Journal of Geophysical Research: Oceans*,
639 **129** (11), e2024JC021 399, doi:10.1029/2024JC021399.